Theranostic Nanoparticles with Controlled Release of Gemcitabine for Targeted Therapy and MRI of Pancreatic Cancer

Gee Young Lee,[†,§] Wei Ping Qian,[†] Liya Wang,[‡] Yongqiang Andrew Wang,[⊥] Charles A. Staley,[†] Minati Satpathy,[†] Shuming Nie,[§] Hui Mao,[‡,*] and Lily Yang[†,‡,*]

[†]Departments of Surgery, [‡]Radiology and Imaging Sciences, and [§]Biomedical Engineering, Emory University School of Medicine, Atlanta, Georgia 30322, United States and [⊥]Ocean NanoTech, LLC, Springdale, Arkansas 72764, United States

ABSTRACT The tumor stroma in human cancers significantly limits the delivery of therapeutic agents into cancer cells. To develop an effective therapeutic approach overcoming the physical barrier of the stroma, we engineered urokinase plasminogen activator receptor (uPAR)-targeted magnetic iron oxide nanoparticles (IONPs) carrying chemotherapy drug gemcitabine (Gem) for targeted delivery into uPAR-expressing tumor and stromal cells. The uPAR-targeted nanoparticle construct, ATF-IONP-Gem, was prepared by conjugating IONPs with the amino-terminal fragment (ATF) peptide of the receptor-binding domain of uPA, a natural ligand of uPAR, and Gem *via* a lysosomally cleavable tetrapeptide linker. These theranostic nanoparticles enable intracellular release of Gem following receptor-mediated endocytosis of ATF-IONP-Gem into tumor cells and also provide contrast enhancement in magnetic resonance imaging (MRI) of tumors. Our results demonstrated the pH- and lysosomal enzyme-dependent release of gemcitabine, preventing the drug from enzymatic degradation. Systemic administrations of ATF-IONP-Gem significantly inhibited the growth of orthotopic human pancreatic cancer xenografts in nude mice. With MRI contrast enhancement by IONPs, we detected the presence of IONPs in the residual tumors following the treatment, suggesting the possibility of monitoring drug delivery and assessing drug-resistant tumors by MRI. The theranostic ATF-IONP-Gem nanoparticle has great potential for the development of targeted therapeutic and imaging approaches that are capable of overcoming the tumor stromal barrier, thus enhancing the therapeutic effect of nanoparticle drugs on pancreatic cancers.

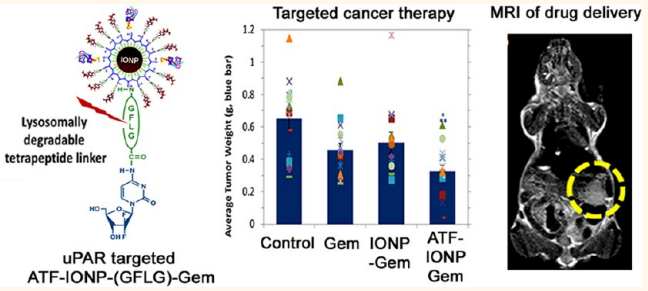

KEYWORDS: targeted cancer therapy · theranostic nanoparticle · uPAR · pancreatic cancer · gemcitabine · controlled drug release · magnetic resonance imaging · drug delivery

Pancreatic cancer is the fourth leading cause of cancer death in America. Most patients have tumors that cannot be surgically resected, so chemotherapy and radiotherapy are the only options for these patients. High resistance to therapy is a major challenge in treating pancreatic cancer.[1,2] Increasing evidence shows that the pancreatic tumor microenvironment includes several barriers to treatment. The enriched tumor stromal component and disorganized vasculature of pancreatic cancer tissues make it extremely difficult to deliver a sufficient amount of therapeutic agents into pancreatic cancers.[3−5] Recent studies have shown that the tumor stroma promotes proliferation, invasion, metastasis, and chemoresistance in pancreatic cancer cells.[3,4,6−8] In the clinical management of pancreatic cancer patients, timely assessment of therapeutic response to a given therapy is critical for making treatment decisions. Therefore, a system combining effective drug delivery and treatment monitoring is particularly desirable to improve the survival of pancreatic cancer patients. While nanomaterials and nanotechnologies provide new strategies to deliver therapeutics to targeted tumors, their clinical applications depend on the ability to deliver nanoparticles preferentially into the tumor mass. Tumor targeted delivery can

* Address correspondence to lyang02@emory.edu; hmao@emory.edu.

Received for review September 19, 2012 and accepted February 12, 2013.

Published online February 12, 2013
10.1021/nn3043463

© 2013 American Chemical Society

increase bioavailability of the drug to the tumor tissues while reducing systemic toxicity. Our previous studies have shown that urokinase plasminogen activator receptor (uPAR)-targeted nanoparticles can improve the specificity and cellular internalization of nanoparticles, providing a promising approach for the targeted delivery of imaging nanoparticle probes or therapeutic agents into cancer cells, tumor endothelial cells, and tumor macrophages.[9−11] Urokinase plasminogen activator (uPA) is a serine protease that regulates multiple pathways involved in matrix degradation, cell motility, metastasis, and angiogenesis.[12−14] Over 86% of pancreatic cancer tissues have high levels of uPAR expression in tumor cells, tumor endothelial cells, and tumor stromal fibroblasts and macrophages.[15,16] In contrast, its expression is not found in the normal pancreas or in pancreatic tissues with chronic pancreatitis.[15,16] uPAR is an excellent cell receptor for targeted drug delivery since the receptor-mediated cell internalization can efficiently facilitate delivery of the drugs into cancer cells.[17−19] In addition, cytotoxic effects from drugs on tumor stromal fibroblasts and endothelial cells, which have a high level of uPAR expression, can break down the tumor stromal barrier, leading to increased drug delivery efficiency and enhancing the therapeutic response through its antiangiogenesis effect.[20,21]

Magnetic iron oxide nanoparticles (IONPs) are a biocompatible and biodegradable nanoparticle platform for developing molecular imaging probes for targeted magnetic resonance imaging (MRI) and drug delivery.[22−25] IONPs are excellent candidates for developing theranostic nanoparticles that can increase the intracellular drug concentration in pancreatic cancer cells and tumor environment while producing MRI contrast for monitoring drug delivery and therapeutic response.

To develop effective approaches for pancreatic cancer therapy, we engineered a multifunctional theranostic IONP platform combining the imaging capability and receptor specificity of the nanoparticles with novel designs for drug delivery to overcome the physical and intrinsic barriers that confer drug resistance in pancreatic cancer. Our design is based on a tetrapeptide (GFLG) linker that is sensitive to a lysosomal cystein protease, cathepsin B,[26−28] for conjugating gemcitabine (Gem), a chemotherapeutic drug commonly used for pancreatic cancer therapy. This lysosomally enzymatic release strategy takes advantage of the increased level of cathepsin B in pancreatic cancer cells reported recently.[29−31] The amino-terminal fragment (ATF) peptides of uPA, which target to uPAR, were conjugated on the surface of IONPs. We found that ATF-IONP-Gem maintains uPAR targeting as previously reported.[10] Results from the current study show that Gem is released only after receptor-mediated internalization into the endosomes and lysosomes. Systemic delivery of uPAR-targeted theranostic ATF-IONP-Gem

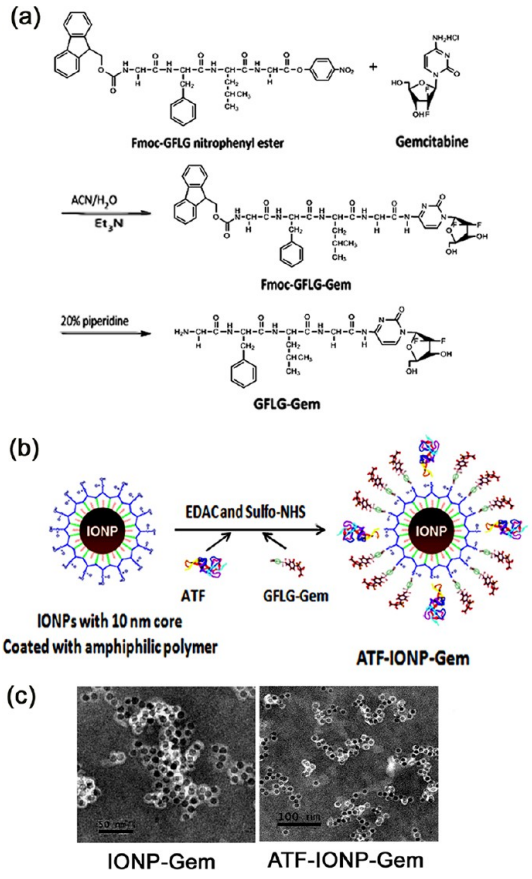

Figure 1. Schematic of the preparation of ATF-IONP-Gem. (a) Synthetic scheme of GFLG-Gem conjugates. (b) Diagram of the conjugation of ATF peptides and GFLG-Gem conjugates to IONPs. (c) Transmission electron microscopy (TEM) images of nontargeted IONP-Gem and targeted ATF-IONP-Gem with negative staining.

significantly reduced the growth of pancreatic tumors in an orthotopic human pancreatic cancer xenograft model. Furthermore, the drug delivery and response to therapy could be monitored by MRI.

RESULTS AND DISCUSSION

Preparation and Characterization of uPAR-Targeted ATF-IONP-Gem. Magnetic IONPs with a uniform core size of 10 nm were synthesized using a method reported previously.[32] Gem, a hydrophilic drug, was conjugated on the polymer surface of the IONPs *via* a Gly-Phe-Leu-Gly (GFLG) tetrapeptide linker (Figure 1). Due to species specificity of the targeting ligand ATF in binding to its cellular receptor, we conjugated a mixture of human and mouse ATF peptides to a single IONP, to ensure ATF-IONP targeting of both human tumor cells and mouse-derived tumor stromal cells in human tumor xenograft models in nude mice. Human and murine recombinant ATF peptides were conjugated to the IONPs at an equal molar ratio. As evaluated by Bradford protein assay, each ATF-IONP-Gem complex contains about 13 ATF peptides. HPLC analysis showed that approximately 570 or 580 GFLG-Gem molecules were

TABLE 1. Characteristics of Nontargeted IONP-Gem and uPAR-Targeted ATF-IONP-Gem

sample	coupling molar ratio[a] (IONPs:ATF:Gem)	hydrodynamic particle size[b] (nm)
IONPs		22.2
IONP-Gem	1:0:580	49.9
ATF-IONP-Gem	1:13:570	65.9

[a] Amount of ATF peptides or gemcitabine molecules was evaluated by Bradford assay or HPLC analysis, respectively. [b] Particle size was measured by a Zetasizer Nano ZS90.

bound to the surface of each IONP in ATF-IONP-Gem or IONP-Gem (Table 1). After conjugation with GFLG-Gem and ATF peptides, the hydrodynamic size of ATF-IONP-Gem increased from 22 nm of the original amphiphilic polymer coated IONPs to 66 nm, determined by dynamic light scattering (DLS) measurement. In comparison, the size of nontargeted IONP-Gem is 49.9 nm (Table 1).

The nanoparticle−drug conjugates were further characterized by transmission electron microscopy (TEM). TEM images show that IONP-Gem and ATF-IONP-Gem retained uniform core size after surface functionalization with the targeting ligand and therapeutic agent (Figure 1c and Figure S1). Negatively stained TEM images revealed a layer of surface modifications on the IONPs (Figure 1c). With the amphiphilic polymer coating and conjugation of GFLG-Gem molecules and ATF peptides, the particle size of ATF-IONP-Gem estimated from TEM images is about 25 to 30 nm, which is significantly smaller than the hydrodynamic particle size measured by DLS. Since the hydrodynamic particle size measurement is affected by surface charges and modifications, it is likely that the particle size measured by TEM represents the actual size of the nanoparticle.

Next, we examined MR relaxation properties of the ATF-IONP-Gem by measuring r_1 and r_2 relaxivities at the field strength of 3 T. Our results showed that the magnetic IO nanocrystal used in this study has strong effects on shortening both longitudinal T_1 and transverse T_2 times. By fitting the values of $1/T_1$ or $1/T_2$ at different concentrations of IONPs, the relaxivities r_1 and r_2 were determined as 1.5 and 195 $mM^{-1}\cdot s^{-1}$, respectively.

The stability of ATF-IONP-Gem was further examined under biologically relevant conditions. ATF-IONP-Gem was incubated in PBS buffer containing 20% or 50% fetal bovine serum at 37 °C for 6 to 24 h. The hydrodynamic size of the particle was measured at different time points. Our results showed that there was no significant change in the hydrodynamic sizes of IONP, IONP-Gem, or ATF-IONP-Gem after incubation in 20% serum for over 24 h and 50% serum for 6 h (Figure S2). However, the particle sizes gradually increased after incubation in 50% serum for more than 6 h and reached 120 to 130 nm at 24 h. This increase may be due to the formation of small IONP aggregates and nonspecific binding of serum proteins to the IONPs. However, the increased size is still less than 200 nm, which is considered the desirable size range for targeted delivery of nanoparticles into tumor.[33]

Controlled Release of Gemcitabine from ATF-IONP-Gem. One of the most important aspects of anticancer drug conjugated nanoparticles is their ability to release the conjugated drugs intracellularly. We investigated whether the GFLG peptide linker can be cleaved by a lysosomal enzyme, cathepsin B, to release Gem under conditions similar to the lysosomes in cells (Figure 2a). ATF-IONP-Gem or IONP-Gem was dispersed in solutions in different pH conditions with or without cathepsin B. A collagenase that does not recognize the GFLG peptide linker was used as a negative control. Results from HPLC analysis, shown in Figure 2a, revealed that the peak of Gem was detected only in the presence of cathepsin B. Under acidic conditions (pH 5.5), 1.5 to 2 times more drugs were released from ATF-IONP-Gem or IONP-Gem compared to physiological conditions (pH 7.4). Specifically, incubation of ATF-IONP-Gem or IONP-Gem at pH 7.4 with cathepsin B led to 40% or 54% release of Gem molecules conjugated to the nanoparticles, respectively. At pH 5.5 and in the presence of cathepsin B, 78% of the conjugated Gem in IONP-Gem and 82% of Gem in ATF-IONP-Gem were released from the nanoparticle-Gem. Importantly, conjugation of ATF peptides to IONPs did not affect the efficiency of drug release (Figure 2b). However, Gem was not released after incubating ATF-IONP-Gem with a nonspecific collagenase for 24 h. Our results confirmed that Gem, which is linked to the IONPs through the GFLG linker peptide, can be conditionally released from conjugated IONPs in the presence of cathepsin B and under mild acidic conditions, which resembles the conditions in intracellular vesicles such as endosomes (pH 5.5−6.0) and lysosomes (pH 4.5−5.0).

Targeted Delivery of ATF-IONP-Gem into Pancreatic Cancer Cells. uPAR-overexpressing MIA PaCa-2 human pancreatic cancer cells were incubated with 10 to 100 nM nontargeted IONPs, IONP-Gem, or ATF-IONP-Gem for 4 h. After washing unbound IONPs, cells were fixed for Prussian blue staining to detect the binding and internalization of the IONPs. As shown in Figure 3a and b, uPAR-targeting markedly increased the amount of ATF-IONP-Gem in the pancreatic cancer cells in a concentration-dependent manner compared to IONPs without targeting. Cells incubated with nontargeted IONP-Gem showed only a low level of IONP uptake even at a high IONP-Gem concentration (100 nM) (Figure 3b). After Prussian blue staining, cells were collected from the tissue culture wells, and the levels of Prussian blue staining intensity in cell lysates were examined using an absorbance of 680 nm for the blue staining. The cells treated with ATF-IONP-Gem had 3- to 7-fold higher

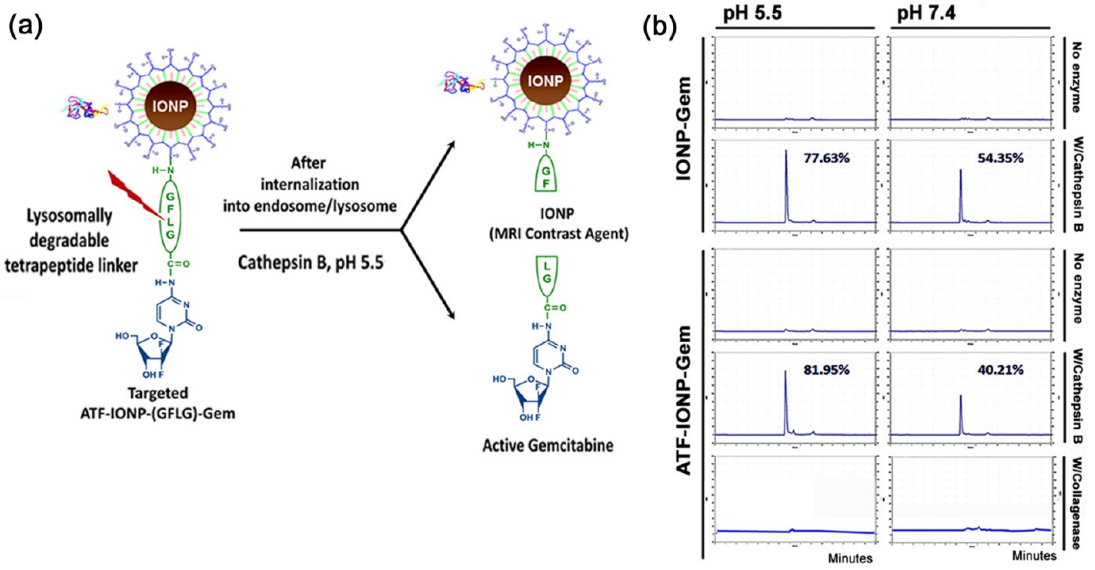

Figure 2. Drug release condition and efficiency. (a) Schematic diagram of gemcitabine release from ATF-IONP-Gem. (b) HPLC chromatograms of the amounts of gemcitabine released from nontargeted IONP-Gem (upper) or uPAR-targeted ATF-IONP-Gem (lower). Both nanoparticles were incubated in the presence of 1 μM cathepsin B or without enzyme at pH 5.5 (left column) or pH 7.4 (right column) for 24 h. 1 μM of a nonspecific collagenase was used as a negative control. The amount of released gemcitabine was measured by HPLC. The percentage of release was calculated from the total amount of conjugated gemcitabine molecules on the nanoparticles.

levels of Prussian blue staining compared with IONP or IONP-Gem, respectively (Figure 3a).

Cytotoxic Effect of ATF-IONP-Gem on Pancreatic Cancer Cells. To evaluate the feasibility of using uPAR-targeted ATF-IONP-Gem to treat pancreatic cancer, we compared the anticancer effects of free Gem and nontargeted and targeted IONPs using MIA PaCa-2 human pancreatic cancer cells. Cells were incubated with free Gem, IONP-Gem, or human ATF-IONP-Gem for 4 h. The culture medium was then replaced with fresh medium without the drug or nanoparticle−drug. Cell proliferation assays were performed 72 h following culture to determine the amount of remaining viable cells. Results showed that at Gem-equivalent concentrations of 1, 3, or 5 μM, ATF-IONP-Gem treatment had significantly stronger inhibitory effects on tumor cell growth than Gem or IONP-Gem (Figure 3c, Student's *t* test, $p < 0.01$ for all three Gem concentrations). At a higher Gem concentration of 5 μM, nontargeted IONP-Gem also showed a significantly higher inhibition of tumor cell growth compared with Gem-treated cells. However, ATF-IONP-Gem still displayed a much lower level of viable cells (29%) than the IONP-Gem-treated cells (60%), suggesting targeted cytotoxicity in pancreatic cancer cells (Figure 3c).

Antitumor Effect of ATF-IONP-Gem in an Orthotopic Human Pancreatic Cancer Xenograft Model. The effect of ATF-IONP-Gem on the growth of pancreatic cancer was examined in nude mice bearing orthotopic tumor xenografts derived from the MIA PaCa-2 human pancreatic cancer cell line. Free Gem, ATF-IONP-Gem, and IONP-Gem with 2 mg/kg of a Gem-equivalent dose were administered twice per week for five times. This is a relatively low Gem dose for the efficacy study in mice, compared with the dosage of 30 to 160 mg/kg of Gem biweekly used as conventional chemotherapy in human pancreatic cancer xenograft models in nude mice by previous studies.[34−36] This Gem-equivalent dose is equal to 300 to 400 pmol of IONPs, which are the optimal doses of the targeted IONPs used in our group for tumor targeting and MRI. At the end of the study, mice were sacrificed and tumors were collected to measure the tumor weight (Figure 4a and b). When comparing the average tumor weights of each group, we found that the tumors from mice treated with ATF-IONP-Gem were smaller than those from the mice treated with free Gem or nontargeted IONP-Gem. Statistically significant differences in the averaged tumor weight were observed based on the results of three repeated experiments analyzed by one-way ANOVA ($p < 0.0005$, $n = 16$), modified *t* test, or Welch's *t* test[37,38] (control with no treatment *vs* ATF-IONP-Gem: $p = 0.0002$, Gem *vs* ATF-IONP-Gem: $p = 0.022$, IONP-Gem *vs* ATF-IONP-Gem: $p = 0.018$). In comparison with the nontreated control group, all treated groups showed various degrees of inhibition of tumor growth. Gem-only and nontargeted IONP-Gem were found to inhibit tumor growth by 30% and 23%, respectively. However, there was no statistically significant difference between these two groups ($p = 0.4086$). In contrast, the group treated with ATF-IONP-Gem showed approximately 50% tumor growth inhibition, which was significantly different from the free Gem and nontargeted IONP-Gem groups. Our results demonstrated that *in vivo* uPAR-targeted delivery of Gem using ATF-IONP-Gem is more effective for the treatment of

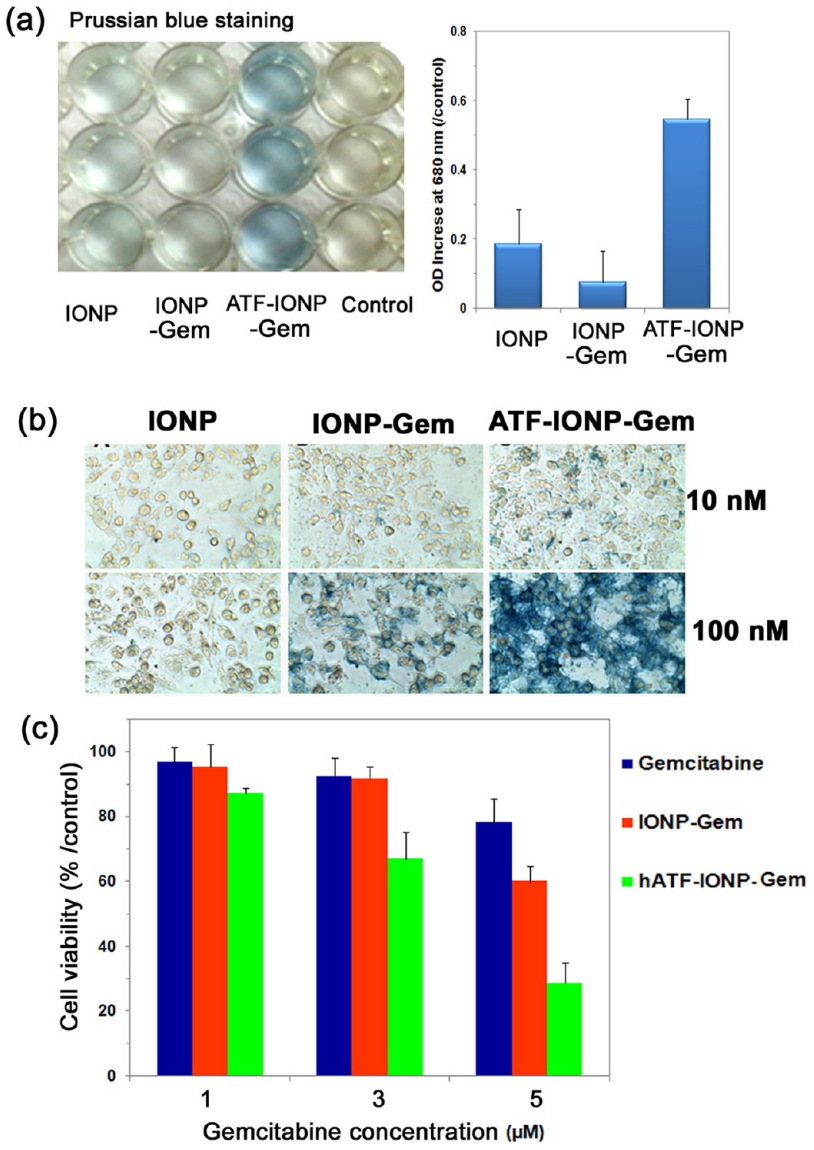

Figure 3. Target specificity and cytotoxicity of ATF-IONP-Gem in a human pancreatic cancer cell line. (a) Prussian blue staining of MIA PaCa-2 cells after incubation with IONPs, IONP-Gem, and ATF-IONP-Gem at 100 nM for 4 h. IONPs in cells were detected as blue-stained cells. Cells were collected, and the intensity of Prussian blue staining in cell lysates was quantified as OD at 680 nm using a microplate reader. (b) Bright field microscopic images of Prussian blue stained cells observed under 40× magnifications. (c) Cell proliferation assay after 4 h treatment followed by 72 h incubation. Crystal violet assay was used to determine viable cells in each well of 96-well tissue culture plates. Data are expressed as the percentage of the untreated control. The values shown are mean ± SD for quadruple samples. Student's *t* test: at 3 μM Gem concentration, no treatment control *vs* ATF-IONP-Gem: $p = 0.0002$, Gem *vs* ATF-IONP-Gem: $p = 0.0002$, IONP-Gem *vs* ATF-IONP-Gem: $p = 0.005$. In 5 μM Gem-treated cells, no treatment control *vs* ATF-IONP-Gen: $p = 1 \times 10^{-6}$, Gem *vs* ATF-IONP-Gem: $p = 0.0002$, IONP-Gem *vs* ATF-IONP-Gem: $p = 0.0003$.

pancreatic cancer compared with the conventional Gem treatment.

Tumor tissue samples were further examined by histological analysis. In H&E-stained paraffin tumor tissue sections, the tumors treated with ATF-IONP-Gem had necrotic areas in both peripheral and central tumor regions (Figure 4c). However, no necrosis was found in the tumors treated with free Gem (Figure 4c). Immunohistochemical staining using an anti Ki-67 antibody, which reacts with the cell proliferation marker Ki-67, revealed a very high level of proliferating cells in the tumor tissue sections of the no treatment group (Figure 4d). We did not detect Ki-67 positive cells in the ATF-IOP-Gem-treated tumor tissue sections (Figure 4d). Additionally, the levels of Ki-67-positive cells were decreased in tumor tissues treated with free Gem or nontargeted IONP-Gem compared to the control with no treatment. A decrease in tumor cell proliferation might be the reason for the tumor growth inhibition observed in those groups (Figure 4a). The enhanced antitumor effect in the ATF-IONP-Gem-treated group may also be due to the inhibition of tumor cell proliferation and increased cell death in the tumor. Histological examination showed

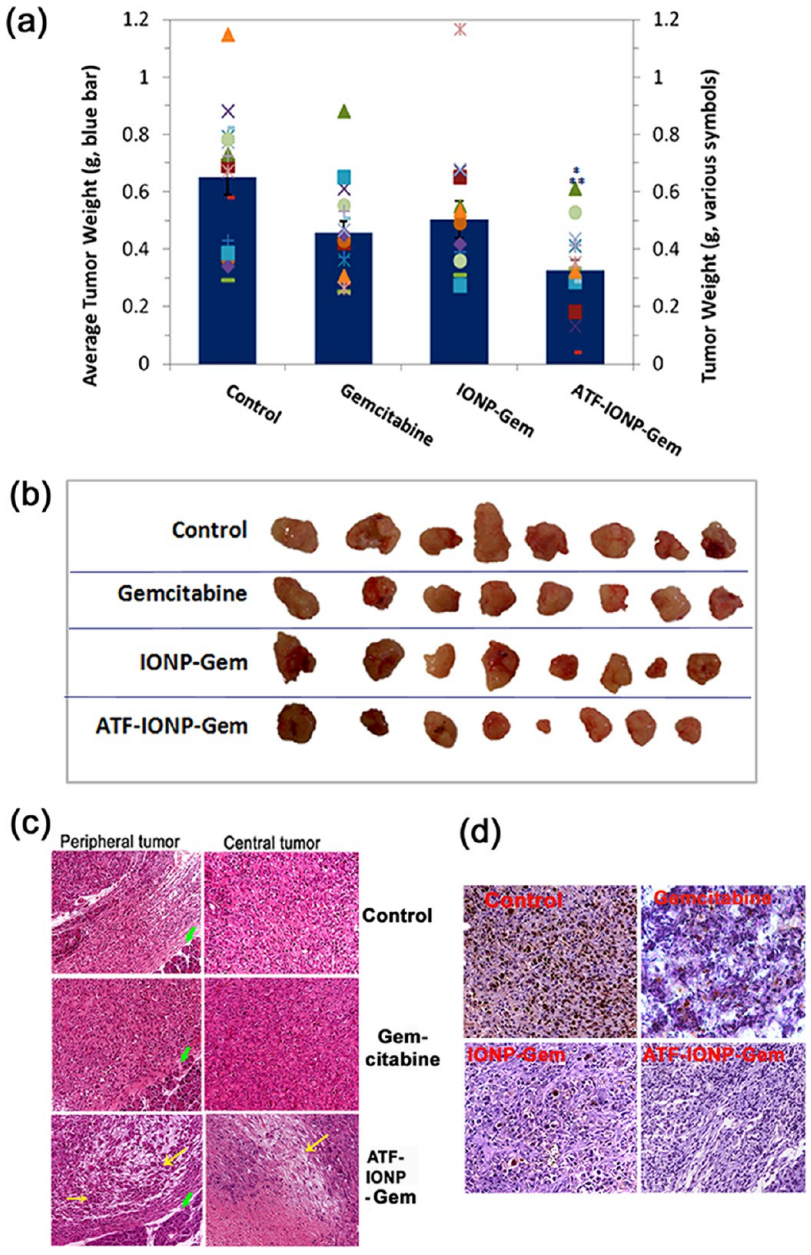

Figure 4. *In vivo* **antitumor effect in an orthotopic human pancreatic cancer xenograft model. Tumor-bearing mice received tail vein injections of 2 mg/kg of the Gem-equivalent dose of various IONPs five times. At the end of the experimental period, tumors were collected and weighed. (a) The mean tumor weights (navy bar) and individual tumor weight distribution of the tumor-bearing mice in each group are shown as colored symbols. Values represent mean ± SD of 16 mice from three repeat studies. *Statistically significant difference *vs* control, one-way ANOVA method: $p < 0.0001$; modified *t* test: $p < 0.0002$. **Statistically significant difference. ATF-IONP-Gem *vs* Gem and IO-Gem groups, one-way ANOVA method: $p < 0.05$; modified *t* test: $p < 0.05$. (b) Representative tumor images of each group after dissection. (c) H&E staining of tumor tissue sections. Yellow arrows: necrotic tumor areas. Green arrows: normal pancreatic acini. (d) Immunohistochemical staining of the cell proliferation marker Ki-67 in tumor tissue sections. Brown: Ki-67-positive tumor cells. Blue: hematoxylin background staining.**

the presence of mouse tumor stroma within the orthotopically implanted human pancreatic cancer xenografts. ATF-IONP-Gem was found in both tumor and stromal-like cells (Figure S3).

Monitoring Targeted Delivery of ATF-IONP-Gem and Tumor Reponses to Therapy by Noninvasive MRI. To determine if the systemic delivery of ATF-IONP-Gem leads to the specific accumulation of the IONPs in tumors, MRI was performed on the tumor-bearing mice before and one and two weeks following the theranostic nanoparticle treatment. Magnetic nanoparticles typically lead to reduced signals in T_2-weighted imaging in the area where nanoparticles accumulate. We found that the MRI signal intensity of T_2-weighted images decreased 24% in the pancreatic tumors of mice that received systemic delivery of ATF-IONP-Gem, from the signal

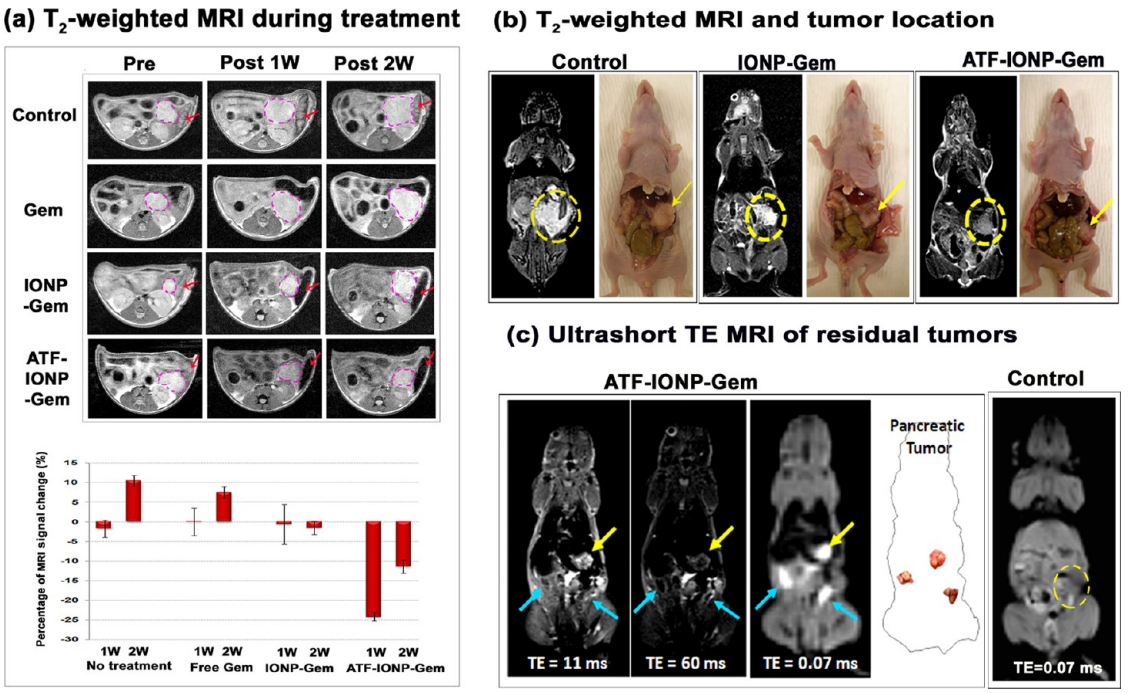

Figure 5. MRI of targeted delivery of ATF-IONP-Gem and tumor response to therapy. (a) Axial T_2-weighted MR images of the tumor-bearing mice before and one week and two weeks after receiving theranostic nanoparticles. Post-treatment images were obtained 48 h following the second (1 week) and fourth (2 weeks) injection. The location and size of the cancer lesions (pink dotted circles) can be seen in the MR images. Red arrows indicate the MRI contrast change in the spleen. The percentage of MRI signal change was obtained using the averaged signal of the tumor before treatment (Pre, 0%) as the baseline. Signal intensity in the muscle was used as the basal level for each image. The bar plot shows the mean and standard deviation of the MRI signal changes ($n = 3$) at three different time points. (b) Coronal T_2-weighted MR images and corresponding bright field (BF) images of the tumor-bearing mice after systemic delivery of nontargeted IONP-Gem or ATF-IONP-Gem. Tumor-bearing mice without nanoparticle treatment were used as controls. Yellow dotted circles and arrows indicate the location of primary tumor lesions in the MR and bright field images, respectively. (c) Comparison of short TE (TE = 11 ms) and long TE T_2-weighted spin−echo (TE = 60 ms) and ultrashort TE (TE = 0.07 ms) MR images from a mouse treated with ATF-IONP-Gem. All MR images were taken at 48 h after the last of five administrations of targeted IONP-Gem. The control UTE image is from a tumor-bearing mouse not receiving nanoparticles. Yellow arrows indicate the location of primary tumor lesions, and blue arrows indicate the secondary tumor lesions due to metastasis.

level obtained before treatment (Figure 5a, Student's t test, $p < 0.01$, post 1 week). However, T_2-weighted MRI showed no significant signal drop in tumors of the mice treated with nontargeted IONP-Gem. Interestingly, MRI signal intensity in T_2-weighted images increased in the tumors of mice receiving no treatment or free Gem. This is likely due to the increased edema resulting from continuous tumor growth or the effect from drug treatment. The presence of edema typically causes MRI signal increase in T_2-weighted imaging (Figure 5a). Indeed, MRI measurement showed significantly increased tumor size in the control mice without treatment and mice treated with free Gem or IONP-Gem, while there was no apparent tumor growth in mice treated with ATF-IONP-Gem (Figure 5a).

At 48 h following the last treatment, mice were examined by T_2-weighted and ultrashort echo time (UTE) MRI. When examining T_2-weighted images of control mice without treatment or mice treated with nontargeted IONP-Gem or targeted ATF-IONP-Gem, a remarkable signal decrease was observed in the area of the tumor from the mice that received ATF-IONP-Gem but not those received IONP-Gem or control mice, suggesting the selective accumulation of the targeted IONPs in the pancreatic tumors. Using the signal intensity of the muscle as a baseline, we found that there was a 4.8-fold signal decrease in the tumors of mice treated with targeted ATF-IONP-Gem compared to the tumors of mice that received nontargeted IONPs (Figure 5b).

It is well recognized that detecting IONPs in tumors located in the peritoneal cavity with conventional T_2-weighted MRI can be difficult due to intrinsically low background signal level in the liver and spleen, causing poor contrast to differentiate signal drop originating from IONPs accumulated in the tumor. To increase the sensitivity and specificity of MRI detection of pancreatic tumor, we applied a UTE MRI method that produces a bright signal from the IONPs, since UTE imaging allows for capturing T_1 contrast from IONPs to generate a bright signal or positive contrast as demonstrated previously.[39] In our experiments, the mice were examined by the UTE MRI scan at the end of the fifth treatments. We found that UTE imaging generated positive contrast enhancements or bright signals in the residual tumors of the mice that received ATF-IONP-Gem.

In the example shown in Figure 5c, the UTE image revealed three tumor lesions with bright signals in the peritoneal cavity of the mouse treated with ATF-IONP-Gem, where reduced signals appeared on a T_2-weighted image in the same locations. Moreover, areas with bright contrasts correlated well with the tumor locations detected in the peritoneal cavity after the animals were sacrificed.

To further confirm the delivery of ATF-IONP-Gem into the tumor tissues, we performed Prussian blue staining on the tumor tissue sections harvested at the end of the treatment. Prussian blue stained cells were found in the tumor tissue sections from the mice treated with targeted ATF-IONP-Gem, but only a very low level of iron positive cells was detected in the tissue sections from mice treated with nontargeted IONP-Gem (Figure 6a and b). Scattered blue-stained cells or cell debris were found in the necrotic areas of the tumor from the ATF-IONP-Gem treated group (Figure 6a). Since MRI contrast rises from IONPs, the strong MRI contrast observed in tumors accumulating ATF-IONP-Gem but not IONP-Gem suggests that targeted theranostic IONPs were delivered into the tumors. Therefore, it is feasible to use MRI to detect the delivery of theranostic nanoparticles into tumors and to monitor tumor responses to treatment and the presence of the residual tumors that are resistant to therapy.

Additionally, biodistribution of ATF-IONP-Gem or nontargeted IONP-Gem was examined based on evaluation of Prussian blue stained normal tissue sections. As expected for systemic delivery of IONPs, we detected the accumulation of both ATF-IONP-Gem and IONP-Gem only in the liver and spleen and not in other normal organs (Figure 6a and b). Therefore, the tail vein injection of uPAR-targeted ATF-IONP-Gem led to the selective delivery of the nanoparticles into tumor tissues as well as nonspecific uptake by the Kupffer cells in the liver and macrophages in the spleen. Since these macrophages are post-mitotic cells, no apparent tissue damage was detected in the liver and spleen after the treatment (Figure S4). We did not find tissue damage in other normal organs, such as the heart, lung, and kidney, after ATF-IONP-Gem treatment (Figure S4). Furthermore, at a 2 mg/kg dose for five

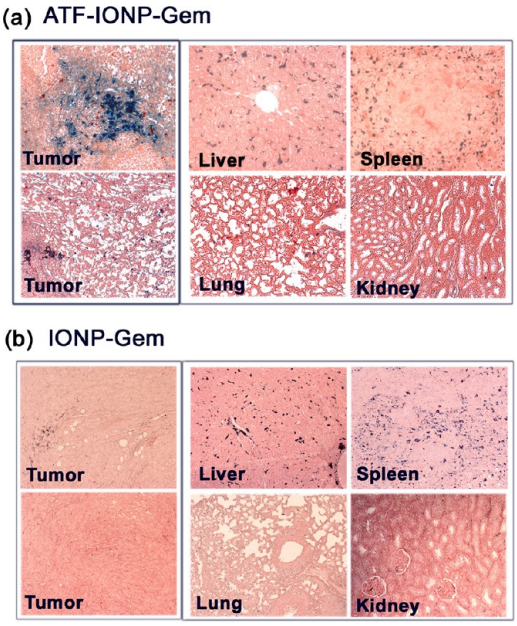

Figure 6. Biodistribution of (a) ATF-IONP-Gem and (b) nontargeted IONP-Gem following systemic treatments. Tumor and normal tissue sections obtained from mice at the end of the five treatments were stained with Prussian blue staining. Blue: IONP positive cells; red: Nuclear Fast Red background staining.

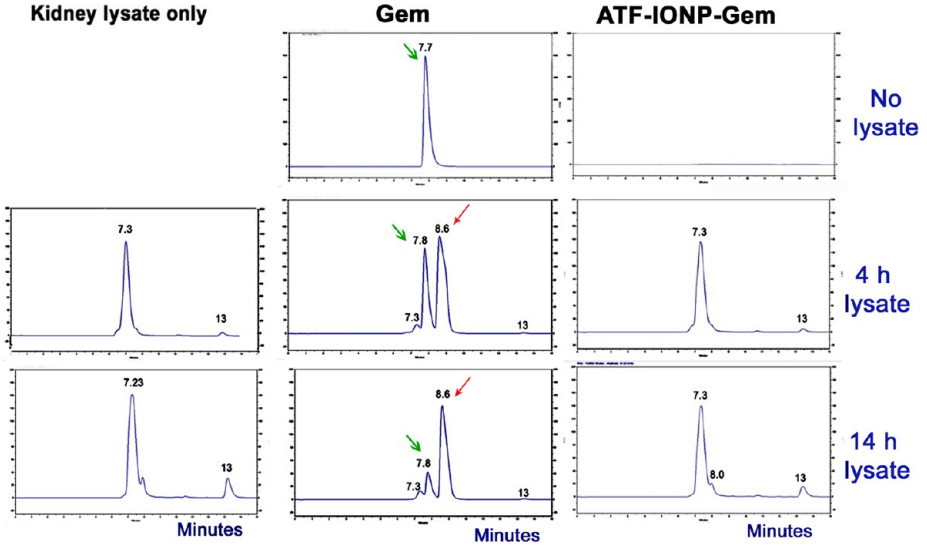

Figure 7. Stability of Gem and ATF-IONP-Gem in mouse kidney tissue lysates. Free Gem and ATF-IONP-Gem were incubated with fresh mouse kidney tissue lysates at 37 °C for 4 to 14 h. Filtrates were analyzed by HPLC. HPLC chromatograms show that the kidney lysate has a peak at 7.2 to 7.3 min. Gem has a peak at 7.7 to 7.8 min (green arrows). Inactivated Gem (dFdU) was found at 8.6 min (red arrow). Chromatogram is not shown after 14 min.

treatments, there was no significant body weight change in all experimental groups (Figure S4). Results of previous studies showed that IONPs were degraded in the endosomes and lysosomes of macrophages.[22] It is likely that ATF-IONP-Gem in the liver and spleen can be degraded inside microphages. Further studies on biodistribution, pharmacokinetics, and pharmacodynamics of ATF-IONP-Gem following systemic administration will provide important information for future translation of the theranostic ATF-IONP-Gem nanoparticles to the treatment of pancreatic cancer patients.

Finally, we compared the stability of free Gem and ATF-IONP-Gem in the presence of cytidine deaminase. It has been shown that the mouse kidney has a high level of cytidine deaminase.[40] Free Gem and ATF-IONP-Gem were incubated with 100% mouse kidney tissue lysates for 4 to 14 h. Supernatant fractions were collected after passing through 3K spin columns and then analyzed by HPLC. We found that free Gem molecules were converted to inactivated 2′,2′-difluorodeoxyuridine (dFdU) by cytidine deaminase after 4 or 14 h incubation with the kidney lysates (Figure 7). However, ATF-IONP-Gem was stable in the mouse kidney lysate at pH 7.4. Gem molecules did not release from the nanoparticles. Therefore, we did not detect either active Gem (2′,2′-difluorodeoxycytidine, dFdC) or inactivated Gem (dFdU) after 4 to 14 h of incubation. Our results suggest that conjugating Gem molecules to IONPs may protect the drug from cytidine deaminase inactivation, resulting in ATF-IONP-Gem having sufficient stability for *in vivo* application as a cancer therapeutic agent. Conjugation of Gem to the peptide linker blocks the amine group and, therefore, has the potential to protect rapid deactivation of the drug molecule by cytidine deaminase in the blood, which occurs within 5 to 15 min following intravenous administration.[34,36] As a result, targeted delivery and enzymatic controlled release of bioactive Gem in tumor cells should increase therapeutic efficacy.

CONCLUSION

uPAR-targeted ATF-IONP-Gem combines an MRI contrast enhancing effect with controlled intratumoral release of the chemotherapeutic agent gemcitabine. While ATF peptides were used for targeting uPAR-overexpressing pancreatic cancer and tumor stromal cells, the lysosomal enzyme-sensitive peptide linker was used to conjugate gemcitabine to the surface of the nanoparticle. This theranostic nanoparticle system not only enables intracellular drug release following receptor-mediated endocytosis for optimized drug action and reduced systemic toxicity but also allows the detection of the nanoparticle−drug accumulation in tumors by MRI. In addition, the strategy of using a drug conjugated nanoparticle carrier makes it possible to prevent gemcitabine from deactivation before intracellularly controlled release *via* enzymatic cleavage. Our results demonstrated specific binding of ATF-IONP-Gem to uPAR-positive pancreatic cancer cells. Furthermore, systemic delivery of ATF-IONP-Gem significantly inhibited tumor growth in an orthotopic human pancreatic cancer xenograft model. We further showed that targeted delivery of the ATF-IONP-Gem and the presence of drug-resistant residual tumors could be detected noninvasively by MRI using both T_2-weighted and T_1-weighted UTE imaging. Magnetic IONP has become an increasingly attractive theranostic nanoparticle platform with the combined capabilities of contrast enhancement in MRI and as a drug carrier for therapeutics. The biological safety of magnetic IONPs has been tested in humans, and nontargeted IONPs have been used in cancer patients for the detection of liver tumors or lymph node metastases.[41,42] The uPAR-targeted theranostic IONP gemcitabine carrier developed in this study is a promising drug delivery nanoparticle platform for the targeted and image-guided therapy of pancreatic cancer.

MATERIALS AND METHODS

Production and Purification of Recombinant Mouse and Human ATF Peptides. A complementary DNA fragment encoding amino acids 1 to 135 of mouse or human uPA was isolated by polymerase chain reaction (PCR) amplification and then was cloned into pET101/D-TOPO (mouse ATF) or pET20b(+) (human ATF) expression vector (Invitrogen, Carlsbad, CA, USA). Recombinant human or mouse ATF peptides were expressed in *E. coli* BL21 (Invitrogen) and purified from bacterial extracts under native conditions using a Ni^{2+} NTA-agarose column (Qiagen, Valencia, CA, USA) using established protocols described previously.[9−11]

Synthesis of GFLG-Gem Conjugates. Triethylamine (7.5 μmol) was added to 9-fluorenylmethoxycarbonyl (Fmoc)-Gly-Phe-Leu-Gly (GFLG)-nitrophenyl ester peptide (6.8 μmol, Boaopharma, Inc., Woburn, MA, USA) in 1.0 mL of acetonitrile. The solution was cooled in an ice bath. Gemcitabine (13.6 μmol, Polymed Therapeutics, Inc., Houston, TX, USA) in 1.0 mL of distilled water was mixed with triethylamine (13.6 μmol). Gemcitabine solution was added to the solution of activated peptide dropwise with stirring over 5 min, and the mixture was allowed to react for an additional 100 min. After removing acetonitrile under reduced pressure, water was added to the remaining solution to a final volume of 1.0 mL. This solution was acidified with 6 M hydrochloric acid to pH 2.0, and the (Fmoc)-GFLG-Gem product was allowed to precipitate at 4 °C. After removing the solvent, the remaining solid was rinsed with 1 mL of 1 M hydrochloric acid. The solid (Fmoc)-GFLG-Gem was dried under vacuum for 24 h to yield a white powder. A 100 μL portion of piperidine was added to the solution of Fmoc-GFLG-Gem conjugates in 0.4 mL of *N*,*N*-dimethylmethanamide (DMF, 20% piperidine, Sigma-Aldrich, St. Louis, MO, USA). After being stirred for 5 min at room temperature, the reaction mixture was placed in an ice salt bath, and acetic acid was immediately added. The aqueous solution was extracted with dichloromethane and lyophilized to obtain GFLG-Gem conjugates.

Preparation of ATF-IONP-Gem. Amphiphilic polymer-coated IONPs with a core size of 10 nm were obtained from Ocean NanoTech, LLC (Springdale, AR, USA). The amphiphilic polymers have carboxyl groups for bioconjugation with amine groups of ATF peptides or GFLG-Gem conjugates. As shown in Figure 1, ATF peptides and GFLG-Gem conjugates were conjugated to the IONPs using ethyl-3-dimethyl amino propyl carbodiimide (EDAC, Sigma-Aldrich) and *N*-hydroxysulfosuccinimide (sulfo-NHS, Sigma-Aldrich) according to the carbodiimide method. Briefly, 108.6 μg of EDAC and 196.9 μg of sulfo-NHS were added to the aqueous solution of 1 mg of IONPs, allowing the activation of IONPs for 15 min. The activated IONPs were reacted with 420.4 μg of GFLG-Gem conjugates alone to produce IONP-Gem. A 200 μg amount of a mixture of mouse and human ATF peptides (1:1, wt/wt) and 420.4 μg of GFLG-Gem conjugates were used to produce ATF-IONP-Gem. The reaction was carried out for 12 h at 4 °C, and the final IONP-(GFLG)-Gem or ATF-IONP-(GFLG)-Gem conjugates in 10 mM borate buffer (pH 8.5) were purified using a magnet separator (Ocean NanoTech, LLC) or Nanosep 100 K column (Pall Corporation, Port Washington, NY, USA). The size and zeta potential of IONP-Gem and ATF-IONP-Gem were measured by a Zeta-sizer Nano (ZS90, Malvern Instruments Ltd., Worcestershire, UK). The core sizes of copolymer-coated and surface-functionalized nanocrystals, *i.e.*, IONP, IONP-Gem, and ATF-IONP-Gem, and thickness of polymer layers were viewed and measured by TEM (Hitachi H-7500 instrument (75 kV)). A drop of diluted solution was put on the grid and air-dried. The grid was then examined by TEM.

Measurement of Release of Gemcitabine by Cathepsin B. A 10 μL sample of IONP-Gem and ATF-IONP-Gem were placed in 90 μL of PBS buffer containing 1 μM cathepsin B (Sigma-Aldrich) at pH 5.5 or 7.4. After incubation at 37 °C for 24 h, IONPs were separated from buffer by Nanosep 100 K column filtration. Detached fragments were isocratically eluted using a reverse-phase HPLC system (Beckman Coulter, Inc., Brea, CA, USA) with acetonitrile and water (20:80, v/v) containing 0.01% TFA at 0.3 mL/min, and detection was performed at 270 nm.

Cell Lines. The MIA PaCa-2 human pancreatic cancer cell line was purchased from American Type Culture Collection (ATCC, Rockville, MD, USA). The cell line was maintained at 37 °C and 5% CO_2 in DMEM (Dulbecco's modified Eagle's medium) supplemented with 1% antibiotics and 10% fetal bovine serum.

Confirmation of the uPAR Target Specificity of ATF-IONP-Gem *in Vitro*. Prussian blue staining for iron was performed to evaluate the specificity of uPAR-targeting peptide ATF-conjugated IONPs to pancreatic cancer cells. In a 24-well cell culture plate, cells were placed and allowed to adhere. At 70−80% confluence, cells were incubated in medium supplemented with 2% fetal bovine serum containing IONPs, IONP-Gem, or ATF-IONP-Gem at 10 and 100 nM IONPs-equivalent concentration for 4 h at 37 °C. Cells were then washed with PBS and fixed with 4% paraformaldehyde for 10 min. To investigate the presence of the IONPs, the fixed cells were exposed to Prussian blue staining solution at an equal part of 10% potassium ferrocyanide, trihydrate (MP Biomedicals, LLC, Solon, OH, USA) and 10% hydrochloric acid at 37 °C for 1 h. After washing with PBS, cells were examined under a microscope and then collected for quantification of the intensity of Prussian blue staining.

Cell Proliferation Assay. A total of 3×10^3 cells were placed in 96-well culture plates and allowed to adhere overnight. Culture medium was then replaced with fresh medium containing free Gem, IONP-Gem, or ATF-IONP-Gem at Gem-equivalent concentrations of 1, 3, and 5 μM. Cells were incubated for 4 h, and the culture medium containing the drug or nanoparticle−drug was removed and replaced with regular culture medium. Cells were cultured for an additional 72 h at 37 °C in a 5% CO_2 tissue culture incubator. The percentage of remaining viable cells was determined by a crystal violet cell proliferation assay. Briefly, cells were fixed with 4% paraformaldehyde, washed with PBS, and then stained with 0.5% crystal violet solution for 20 min at room temperature. After washing in tap water and air-drying, 100 μL of Sorenson's buffer was added to each well to dissolve stained cells. The plate was read at a 570 nm absorbance wavelength using a microplate reader (SpectraMAX Plus 384, Molecular Devices, Sunnyvale, CA, USA). The absorbance value was normalized to the value of the control group to obtain the percentage of viable cells. This experiment was performed in quadruplicate in each treatment group, and similar results were obtained in three separate tests.

Preparation of Orthotopic Human Pancreatic Cancer Xenograft Model. The pancreatic cancer model was prepared by directly injecting 5×10^6 MIA PaCa-2 cells into the pancreas of 7- to 8-week-old female nude mice (Harlan Laboratories, Inc., Indianapolis, IN, USA) using a surgical procedure approved by the Emory University Institutional Animal Care and Use Committee. In 3 to 4 weeks, orthotopically xenografted pancreatic tumors typically reached 5 mm in diameter and were ready for experiments. Animals were randomized into four experimental groups of 5 or 6 mice as follows: control, Gem, nontargeted IONP-Gem, and ATF-IONP-Gem. The mice were treated *via* five tail vein injections at 3- or 4-day intervals. On each treatment day, all groups except for the control group were administered a Gem-equivalent dose of 2 mg/kg of body weight. Control mice received saline buffer injection. The animal study was performed three times under the same conditions, and the results of three separate experiments were combined to analyze values. The body weights of mice were measured and recorded twice a week.

MRI Experiments. MRI experiments were carried out on 3 T MRI scanner (Siemens Tim Trio, Siemens, Erlanen, Germany) or 4.7 T small animal MRI scanner (Oxford Magnet Technology, Oxford, UK). MR relaxation properties of ATF-IONP-Gem were determined by fitting MRI signal changes of aqueous IONP solutions with different iron concentrations to the empirical equations describing longitudinal (T_1) and transverse (T_2) relaxation times. The details of image acquisition and data fitting were described previously.[39] Briefly, for determining r_1 relaxivity, IONP solution phantoms were scanned using a T_1-weighted inversion recovery imaging sequence with variable inversion times. For determining r_2 relaxivity, multiecho T_2-weighted fast spin echo imaging sequences with variable echo times (TE) were used. The signal intensity of each region-of-interest (ROI) selected from the images of each sample and each timing point was measured. The T_1 and T_2 relaxation times were derived from the fitting of measured average signal intensities to nonlinear exponential equations describing signal evolution under T_1- and T_2-weighted imaging conditions. *In vivo* MRI scans were performed on mice in the IONP-Gem- or ATF-IONP-Gem-treated groups before the initial treatment and at 48 h after the last treatment using a volumetric wrist coil. Mice were anesthetized by i.p. administration of a mixture of 100 mg/kg ketamine and 10 mg/kg xylazine and then were immobilized in the coil before being placed in the iso-center of the magnet. Images were obtained in axial and coronal sections using the protocol described previously.[9−11] The imaging sequences included T_2-weighted fast spin echo imaging with repetition time (TR) = 3600 ms, TE = 32 ms, image matrix = 320 × 128, field of view (FOV) = 40 × 120 mm^2, slice thickness = 1 mm, and number of averages = 3; a multiecho spin echo sequence with a TR of 4981 ms and 20 TEs starting at 12.1 ms with increments of 12.1 ms for obtaining T_2 relaxometry maps; and a UTE sequence performed with two different TEs including an ultrashort TE of 0.07 ms and a longer TE of 4.03 ms. TR = 6.59 ms, flip angle = 14°, FOV = 16 × 16 × 16 cm^3, image matrix = 192 × 192 × 192, voxel size = 0.6 × 0.6 × 0.6 mm^3, radial views = 64 000. Images from pre- and post-contrast administration as well as those from control mice and/or experimental mice were compared to evaluate the contrast enhancement by IONP-Gem and ATF-IONP-Gem. Image evaluation was performed using the Image J program (U.S. National Institutes of Health, Bethesda, MD, USA). The regions of interest (ROI) method was used to assess the IONP-induced changes in MRI signal level, contrast, and T_2 values in the tumor and other organs. The signals of the leg or back muscle, which showed little change before and after the injection of IONPs, was used as a baseline for comparison of the signals in ROIs.

Histological Analysis of Tumor Tissues. Paraffin-embedded tissue sections were stained with H&E staining solutions by the standard protocol. Prussian blue staining was used to confirm the presence of IONPs in the tumor and normal tissue sections using our established method.[10,11] Immunohistochemical

staining was performed using a mouse anti-Ki-67 monoclonal antibody (Clone 7B11, Invitrogen) followed by horseradish peroxidase (HRP)-goat-anti-mouse secondary antibody. 3,3′-diaminobenzidine (DAB) substrate solution (Vector Laboratories, Burlingame, CA, USA) was used to detect Ki-67-positive cells.

Stability of ATF-IONP-Gem in the Presence of a High Concentration of Cytidine Deaminase. Free Gem and ATF-IO-Gem were incubated with fresh mouse kidney lysates at 37 °C for 4 and 14 h, and then IONPs and proteins in lysates were separated from the buffer by Nanosep 3 K column filtration. The filtrates were isocratically eluted using a reverse-phase HPLC system (Beckman Coulter, Inc., Brea, CA, USA) with acetonitrile and water (20:80, v/v) containing 0.01% trifluoroacetic acid at 0.3 mL/min, and detection was performed at 270 nm.

Statistical Analysis. Statistically significant differences ($p < 0.05$) between groups with respect to cell viability in tumor cells and tumor weights in *in vivo* studies were determined using the one-way ANOVA test, the standard Student's *t* test, and the modified *t* test.

Conflict of Interest: The authors declare no competing financial interest.

Acknowledgment. We thank Dr. Xiangxue Gao for assistance with the statistical analysis of the *in vivo* results. This research was supported by the following NIH grants: U01CA151810 (L.Y. and H.M.), R01CA154846 (H.M. and L.Y.), Project 3 of P50CA128301 (H.M. and L.Y.), and R01CA154129A01 (L.Y.), and the Nancy Panoz Chair of Surgery in Cancer Research Endowment.

Supporting Information Available: This material is available free of charge via the Internet at http://pubs.acs.org

REFERENCES AND NOTES

1. Willett, C. G.; Czito, B. G.; Bendell, J. C.; Ryan, D. P. Locally Advanced Pancreatic Cancer. *J. Clin. Oncol.* **2005**, *23*, 4538–4544.
2. Warshaw, A. L.; Fernandez-del Castillo, C. Pancreatic Carcinoma. *N. Engl. J. Med.* **1992**, *326*, 455–465.
3. Hwang, R. F.; Moore, T.; Arumugam, T.; Ramachandran, V.; Amos, K. D.; Rivera, A.; Ji, B.; Evans, D. B.; Logsdon, C. D. Cancer-Associated Stromal Fibroblasts Promote Pancreatic Tumor Progression. *Cancer Res.* **2008**, *68*, 918–926.
4. Mahadevan, D.; Von Hoff, D. D. Tumor-Stroma Interactions in Pancreatic Ductal Adenocarcinoma. *Mol. Cancer Ther.* **2007**, *6*, 1186–1197.
5. Kalluri, R.; Zeisberg, M. Fibroblasts in Cancer. *Nat. Rev. Cancer* **2006**, *6*, 392–401.
6. Apte, M. V.; Park, S.; Phillips, P. A. Desmoplastic Reaction in Pancreatic Cancer: Role of Pancreatic Stellate Cells. *Pancreas* **2004**, *29*, 179–187.
7. Lopes, R. B.; Gangeswaran, R.; McNeish, I. A.; Wang, Y.; Lemoine, N. R. Expression of the IAP Protein Family Is Dysregulated in Pancreatic Cancer Cells and Is Important for Resistance to Chemotherapy. *Int. J. Cancer* **2007**, *120*, 2344–2352.
8. Miyamoto, H.; Murakami, T.; Tsuchida, K.; Sugino, H.; Miyake, H.; Tashiro, S. Tumor-Stroma Interaction of Human Pancreatic Cancer: Acquired Resistance to Anticancer Drugs and Proliferation Regulation Is Dependent on Extracellular Matrix Proteins. *Pancreas* **2004**, *28*, 38–44.
9. Yang, L.; Cao, Z.; Sajja, H. K.; Mao, H.; Wang, L.; Gene, H.; Xu, H.; Jiang, T.; Wood, W. C.; Nie, S.; *et al*. Development of Receptor Targeted Magnetic Iron Oxide Nanoparticles for Efficient Drug Delivery and Tumor Imaging. *J. Biomed. Nanotechnol.* **2008**, *4*, 1–11.
10. Yang, L.; Mao, H.; Cao, Z.; Wang, Y. A.; Peng, X.; Wang, X.; Sajja, H. K.; Wang, L.; Duan, H.; Ni, C.; *et al*. Molecular Imaging of Pancreatic Cancer in an Animal Model Using Targeted Multifunctional Nanoparticles. *Gastroenterology* **2009**, *136*, 1514–1525.
11. Yang, L.; Peng, X. H.; Wang, Y. A.; Wang, X.; Cao, Z.; Ni, C.; Karna, P.; Zhang, X.; Wood, W. C.; Gao, X.; *et al*. Receptor-Targeted Nanoparticles for *in Vivo* Imaging of Breast Cancer. *Clin. Cancer. Res.* **2009**, *15*, 4722–4732.
12. Blasi, F.; Carmeliet, P. uPAR: a Versatile Signalling Orchestrator. *Nat. Rev. Mol. Cell Biol.* **2002**, *3*, 932–943.
13. Tan, X.; Egami, H.; Nozawa, F.; Abe, M.; Baba, H. Analysis of the Invasion-Metastasis Mechanism in Pancreatic Cancer: Involvement of Plasmin(ogen) Cascade Proteins in the Invasion of Pancreatic Cancer Cells. *Int. J. Oncol.* **2006**, *28*, 369–374.
14. He, Y.; Liu, X. D.; Chen, Z. Y.; Zhu, J.; Xiong, Y.; Li, K.; Dong, J. H.; Li, X. Interaction between Cancer Cells and Stromal Fibroblasts Is Required for Activation of the uPAR-uPA-MMP-2 Cascade in Pancreatic Cancer Metastasis. *Clin. Cancer Res.* **2007**, *13*, 3115–3124.
15. Cantero, D.; Friess, H.; Deflorin, J.; Zimmermann, A.; Brundler, M. A.; Riesle, E.; Korc, M.; Buchler, M. W. Enhanced Expression of Urokinase Plasminogen Activator and its Receptor in Pancreatic Carcinoma. *Br. J. Cancer* **1997**, *75*, 388–395.
16. Chen, Y.; Zheng, B.; Robbins, D. H.; Lewin, D. N.; Mikhitarian, K.; Graham, A.; Rumpp, L.; Glenn, T.; Gillanders, W. E.; Cole, D. J.; *et al*. Accurate Discrimination of Pancreatic Ductal Adenocarcinoma and Chronic Pancreatitis Using Multimarker Expression Data and Samples Obtained by Minimally Invasive Fine Needle Aspiration. *Int. J. Cancer* **2007**, *120*, 1511–1517.
17. Hoyer-Hansen, G.; Ploug, M.; Behrendt, N.; Ronne, E.; Dano, K. Cell-Surface Acceleration of Urokinase-Catalyzed Receptor Cleavage. *Eur. J. Biochem.* **1997**, *243*, 21–26.
18. Rajagopal, V.; Kreitman, R. J. Recombinant Toxins That Bind to the Urokinase Receptor Are Cytotoxic without Requiring Binding to the Alpha(2)-Macroglobulin Receptor. *J. Biol. Chem.* **2000**, *275*, 7566–7573.
19. Stahl, A.; Mueller, B. M. The Urokinase-Type Plasminogen Activator Receptor, a GPI-Linked Protein, Is Localized in Caveolae. *J. Cell Biol.* **1995**, *129*, 335–344.
20. Nielsen, B. S.; Rank, F.; Illemann, M.; Lund, L. R.; Dano, K. Stromal Cells Associated with Early Invasive Foci in Human Mammary Ductal Carcinoma *in Situ* Coexpress Urokinase and Urokinase Receptor. *Int. J. Cancer* **2007**, *120*, 2086–2095.
21. Li, H.; Lu, H.; Griscelli, F.; Opolon, P.; Sun, L. Q.; Ragot, T.; Legrand, Y.; Belin, D.; Soria, J.; Soria, C.; *et al*. Adenovirus-Mediated Delivery of a uPA/uPAR Antagonist Suppresses Angiogenesis-Dependent Tumor Growth and Dissemination in Mice. *Gene Ther.* **1998**, *5*, 1105–1113.
22. Pouliquen, D.; Le Jeune, J. J.; Perdrisot, R.; Ermias, A.; Jallet., P. Iron Oxide Nanoparticles for Use as an MRI Contrast Agent: Pharmacokinetics and Metabolism. *Magn. Reson. Imaging* **1991**, *9*, 275–283.
23. Lee, J. H.; Huh, Y. M.; Jun, Y. W.; Seo, J. W.; Jang, J. T.; Song, H. T.; Kim, S.; Cho, E. J.; Yoon, H. G.; Suh, J. S.; *et al*. Artificially Engineered Magnetic Nanoparticles for Ultra-Sensitive Molecular Imaging. *Nat. Med.* **2007**, *13*, 95–99.
24. Moore, A.; Medarova, Z.; Potthast, A.; Dai, G. *In Vivo* Targeting of Underglycosylated MUC-1 Tumor Antigen Using a Multimodal Imaging Probe. *Cancer Res.* **2004**, *64*, 1821–1827.
25. Nasongkla, N.; Bey, E. J.; Ren, H.; Ai, Khemtong, C.; Guthi, J. S.; Chin, S. F.; Sherry, A. D.; Boothman, D. A.; Gao, J. Multifunctional Polymeric Micelles as Cancer-Targeted, MRI-Ultrasensitive Drug Delivery Systems. *Nano Lett.* **2006**, *6*, 2427–2430.
26. Lu, Z. R.; Kopecková, P.; Kopecek, J. Polymerizable Fab′ Antibody Fragments for Targeting of Anticancer Drugs. *Nat. Biotechnol.* **1999**, *17*, 1101–1104.
27. Naqvi, S. A.; Matzow, T.; Finucane, C.; Nagra, S. A.; Ishfaq, M. M.; Mather, S. J.; Sosabowski, J. Insertion of a Lysosomal Enzyme Cleavage Site into the Sequence of a Radiolabeled Neuropeptide Influences Cell Trafficking *in Vitro* and *in Vivo*. *Cancer Biother. Radiopharm.* **2010**, *25*, 89–95.
28. Lammers, T.; Subr, V.; Ulbrich, K.; Peschke, P.; Huber, P. E.; Hennink, W. E.; Storm, G. Simultaneous Delivery of Doxorubicin and Gemcitabine to Tumors *in Vivo* Using Prototypic Polymeric Drug Carriers. *Biomaterials* **2009**, *30*, 3466–3475.
29. Niedergethmann, M.; Wostbrock, B.; Sturm, J. W.; Willeke, F.; Post, S.; Hildenbrand, R. Prognostic Impact of Cysteine

Proteases Cathepsin B and Cathepsin L in Pancreatic Adenocarcinoma. *Pancreas* **2004**, *29*, 204–211.
30. von Burstin, J.; Eser, S.; Seidler, B.; Meining, A.; Bajbouj, M.; Mages, J.; Lang, R.; Kind, A. J.; Schnieke, A. E.; Schmid, R. M.; *et al*. Highly Sensitive Detection of Early-Stage Pancreatic Cancer by Multimodal Near-Infrared Molecular Imaging in Living Mice. *Int. J. Cancer* **2008**, *123*, 2138–2147.
31. Esera, S.; Messera, M.; Eserb, P.; von Werdera, A.; Seidlera, B.; Bajbouja, M.; Vogelmanna, R.; Meininga, A.; von Burstina, J.; Algüla, H.; *et al*. *In Vivo* Diagnosis of Murine Pancreatic Intraepithelial Neoplasia and Early-Stage Pancreatic Cancer by Molecular Imaging. *Proc. Natl. Acad. Sci. U.S.A.* **2011**, *108*, 9945–9950.
32. Yu, W. W.; Falkner, J. C.; Yavuz, C. T.; Colvin, V. L. Synthesis of Monodisperse Iron Oxide Nanocrystals by Thermal Decomposition of Iron Carboxylate Salts. *Chem. Commun. (Cambridge, U.K.)* **2004**, *20*, 2306–2307.
33. Gaumet, M.; Vargas, A.; Gurny, R.; Delie, F. Nanoparticles for Drug Delivery: The Need for Precision in Reporting Particle Size Parameters. *Eur. J. Pharm. Biopharm.* **2008**, *69*, 1–9.
34. Merriman, R. L; Hertel, L. W.; Schultz, R. M.; Houghton, P. J.; Houghton, J. A.; Rutherford, R. G.; Tanzer, L. R.; Boder, G. B.; Grindey, G. B. Comparison of the Antitumor Activity of Gemcitabine and Ara-C in a Panel of Human Breast, Colon, Lung and Pancreatic Xenograft Models. *Invest. New Drugs* **1996**, *14*, 243–247.
35. Hermann, P. C.; Huber, S. L.; Herrler, T.; Aicher, A.; Ellwart, J. W.; Guba, M.; Bruns, C. J.; Heeschen, C. Distinct Populations of Cancer Stem Cells Determine Tumor Growth and Metastatic Activity in Human Pancreatic Cancer. *Cell Stem Cell* **2007**, *1*, 313–323.
36. Hilbig, A.; Oettle, H. G. Gemcitabine in the Treatment of Metastatic Pancreatic Cancer. *Expert Rev. Anticancer Ther.* **2008**, *8*, 511–523.
37. Welch, B. L. The Generalization of "Student's" Problem When Several Different Population Variances Are Involved. *Biometrika* **1947**, *34*, 28–35.
38. Sawilowsky, S. S. Fermat, Schubert, Einstein, and Behrens-Fisher: The Probable Difference between Two Means When $\sigma_1^2 \neq \sigma_2^2$. *J. Mod. Appl. Stat. Methods* **2002**, *1*, 461–472.
39. Zhang, L.; Zhong, X.; Wang, L.; Chen, H.; Wang, Y. A.; Yeh, J.; Yang, L.; Mao, H. T_1-Weighted Ultrashort Echo Time Method for Positive Contrast Imaging of Magnetic Nanoparticles and Cancer Cells Bound with the Targeted Nanoparticles. *J. Magn. Reson. Imaging* **2011**, *33*, 194–202.
40. Tomchick, R.; Saslaw, L. D.; Waravdekar, V. S. Mouse Kidney Cytidine Deaminase. Purification and Properties. *J. Biol. Chem.* **1968**, *243*, 2534–2537.
41. Harisinghani, M. G.; Barentsz, J.; Hahn, P. F.; Deserno, W. M.; Tabatabaei, S.; van de Kaa, C. H.; de la Rosette, J.; Weissleder, R. Noninvasive Detection of Clinically Occult Lymph-Node Metastases in Prostate Cancer. *N. Engl. J. Med.* **2003**, *348*, 2491–2499.
42. Schultz, J. F.; Bell, J. D.; Goldstein, R. M.; Kuhn, J. A.; McCarty, T. M. Hepatic Tumor Imaging Using Iron Oxide MRI: Comparison with Computed Tomography, Clinical Impact, and Cost Analysis. *Ann. Surg. Oncol.* **1999**, *6*, 691–698.